UC San Diego
UC San Diego Electronic Theses and Dissertations

Title
Optical Layer Determination in Few-Layer Exfoliated MoSe2 and WSe2

Permalink
https://escholarship.org/uc/item/6xf9h3k0

Author
Patz, Jeff

Publication Date
2021

Peer reviewed|Thesis/dissertation

eScholarship.org
Powered by the California Digital Library
University of California

UNIVERSITY OF CALIFORNIA SAN DIEGO

Optical Layer Determination in Few-Layer Exfoliated MoSe2 and WSe2

A Thesis submitted in partial satisfaction of the requirements for the degree Master of Science

in

Electrical and Computer Engineering – Nanoscale Devices and Systems

by

Jeff Patz

Committee in charge:

Professor Leonid Butov, Chair
Professor Zhaowei Liu, Co-Chair
Professor Shayan Mookherjea

2021

Copyright

Jeff Patz, 2021
All rights reserved.

The Thesis of Jeff Patz is approved, and it is acceptable in quality and form for publication on microfilm and electronically.

University of California San Diego

2021

TABLE OF CONTENTS

THESIS APPROVAL PAGE .... *iii*

TABLE OF CONTENTS .... *iv*

LIST OF FIGURES .... *v*

ABSTRACT OF THE THESIS .... *vii*

Chapter 1: Introduction *1*

Chapter 2: Methodology *5*

2.1 Fabrication **5**

2.2 Optical Microscopy **7**

2.3 AFM **7**

2.4 Photoluminescence **8**

Chapter 3: Results *9*

3.1 Optical Imaging **9**

3.2 AFM Measurements **12**

3.3 Photoluminescence Measurements **14**

3.3.1 $MoSe_2$ Photoluminescence Spectra 15

3.3.2 WSe_2 Photoluminescence Spectra 17

3.3.3 Photoluminescence Power Dependence and Crack/Edge Impact 20

Chapter 4: Discussion *22*

4.1 $MoSe_2$ Calibration **22**

4.2 WSe_2 Calibration **24**

Chapter 5: Summary and Recommendations for Further Work *27*

References *29*

Appendix 1: MATLAB Script for Dark Field Image Processing *34*

Appendix 2: MATLAB Script for Spectra Processing *37*

LIST OF FIGURES

Figure 1. (a) momentum space energy diagram for IXs in general TMD system and (b) real space energy diagram for IXs in general TMD system.…………………………………………………………...1

Figure 2. Fabrication process flow for dry-transfer technique…………………………………………….5

Figure 3. Optical setup for photoluminescence measurements.………………………………………..8

Figure 4. (a) Representative bright field image of $MoSe_2$ flake. Upper left hand corner is ML region. (b) the corresponding dark field image. (c) Representative bright field image of WSe_2 flake. Entire flake is monolayer. (d) the corresponding dark field image. All scale bars are 10μm.…………………………...10

Figure 5. Optical microscope images showing (a) Bright field image of the $MoSe_2$ sample with areas of known layer number indicated with different colors. (b) Dark field image of the $MoSe_2$ sample. Both scale bars are 10μm.……………………………………………………………………………………...11

Figure 6. Optical microscope images showing (a) Bright field image of the WSe_2 sample with areas of known layer number indicated with different colors. The six layer regions are three layer regions folded onto themselves. (b) Dark field image of the WSe_2 sample. Both scale bars are 10μm.……………….12

Figure 7. AFM images of $MoSe_2$ flakes transferred onto Si/SiO_2/Graphite/h-BN structure. Representative cross-sections shown as white bars. All scale bars are 2μm. (a) monolayer region, bilayer region, and bright spot (b) bilayer and trilayer regions (c) Four layer region at the tip of the triangle (d) bilayer and thicker regions. …………………………………………………………………...13

Figure 8. AFM images of WSe_2 flakes transferred onto Si/SiO_2/Graphite/h-BN structure. Representative cross-sections shown as white bars. All scale bars are 2μm. (a) trilayer region, (b) four-layer region, (c) four-layer, trilayer, and bilayer regions, (d) four-layer and five-layer regions……14

Figure 9. (a) Defocused illumination image of $MoSe_2$ sample. (b) Spectra of regions labelled in the defocused image. The circle markers are approximately the size of the excitation spot………………17

Figure 10. (a) Defocused illumination image of WSe_2 sample. (b) Spectra of regions labelled in the defocused image. The circle markers are approximately the size of the excitation spot………………19

Figure 11. Power dependence of (a) $MoSe_2$ 1L bright spot and (b) 4L bright spot……………………...20

Figure 12. High energy peak shift when comparing region with a crack near an edge to two regions at the center of the flake far from edges or cracks……………………………………………………..…21

Figure 13. (a) Layer number (AFM step height - offset)/(monolayer thickness) of flakes on $MoSe_2$ sample versus the Dark field contrast (peak/background) and (b) dark field peak intensity……….…..23

Figure 14. Peak energy by layer number (AFM step height - offset)/(monolayer thickness) for the WSe_2 sample. The low energy peak position shifts monotonically with increasing layer number. The set of three points around 3 layers are from three different flakes, demonstrating the moderate level of variation in AFM step heights in comparison to the minimal variation in peak location………………...24

Figure 16. Comparison to measured peak positions by layer number in the literature is in good agreement with this work. As no pristine monolayer region exists on this sample, the 1L peak from this work is the average energy of the high energy peak at each location on the sample…………………..…25

Figure 17. (a) Layer number (AFM step height - offset)/(monolayer thickness) of flakes on WSe_2 sample versus the Dark field contrast (peak/background) and (b) dark field peak intensity…………..…..26

ABSTRACT OF THE THESIS

Optical Layer Determination in Few-Layer Exfoliated MoSe2 and WSe2

by

Jeff Patz

Master of Science in Electrical and Computer Engineering – Nanoscale Devices and Systems

University of California San Diego, 2021

Professor Leonid Butov, Chair
Professor Zhaowei Liu, Co-Chair

Two-dimensional transition metal dichalcogenides (TMDs) provide an exciting platform to study indirect excitons and excitonic devices due to their high exciton binding energy and highly tunable electronic and optical properties. This high binding energy allows for indirect excitons in TMDs to exist at temperatures well above room temperature opening the door for excitonic devices suitable for real-world application. The key to fabricating these multilayer devices is a quick and reliable method for determining the thickness or more appropriately the layer number of TMD flakes used in the fabrication process. While atomic force microscopy (AFM) is a highly accurate

method of layer determination, it can only be carried out after transfer, allocating it to a verification not determination role. Previous works have utilized optical microscopy color contrast for layer determination, but this method is highly substrate dependent and has primarily been investigated on Si/SiO_2, a post transfer substrate. This work establishes dark field microscopy as a suitable fabrication process-integrated method for layer determination in few-layer exfoliated $MoSe_2$ and WSe_2 by correlating dark field microscope images to AFM and photoluminescence measurements.

Chapter 1: Introduction

Spatially indirect excitons (IXs), also known as interlayer excitons, are spatially separated bound electron hole pairs[1]. The separation between the electron and hole layers allows for electrical control of the quasiparticles and allows IXs to achieve long lifetimes, orders of magnitude longer than lifetimes of spatially direct excitons (DXs)[2].

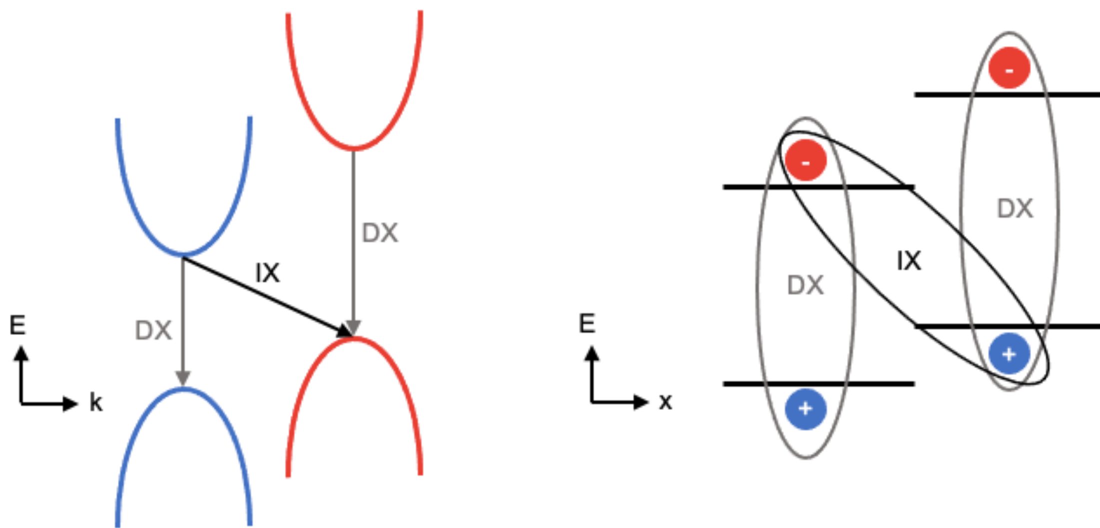

Figure 1. (a) momentum space energy diagram for IXs in general TMD system and (b) real space energy diagram for IXs in general TMD system.

IXs have intrinsic built-in dipole moments. Due to this, their energy can be controlled by voltage. The possibility to control IX energy by voltage and the ability of IXs to propagate over long distances has led to the realization of a variety of tailored voltage-controlled in plane potential landscapes, which are explored in studies of IX transport. These landscapes include excitonic ramps[3-4], excitonic lattices[5-7], excitonic narrow channels[8-9], excitonic conveyers[10], and excitonic split gate devices[11].

IX devices based on the exciton dipole, that is a novel computational state variable, different from established computational state variables such as electron charge in electronic devices, have also been explored. Excitonics then forms an emerging landscape of devices analogous to electronics, photonics, and plasmonics. Potential advantages of excitonic devices include energy-efficient signal processing and seamless coupling of optical inputs and outputs[12]. Experimental proof of principle has been demonstrated for excitonic transistors in GaAs systems[13-14].

Indirect excitons exist at temperatures roughly below E_{ex}/k_B (E_{ex} the exciton binding energy, k_B the Boltzmann constant)[15] and, due to their low binding energies, IXs in GaAs heterostructures exist at low temperatures. E_{ex} is typically ~ 4 meV in GaAs/AlGaAs heterostructures[16] and achieves ~10 meV in GaAs/AlAs heterostructures[17]. The proof of principle for the operation of IX switching devices based on voltage-controlled IX propagation was demonstrated up to ~100 K in GaAs heterostructures[14]. IX devices based on controlled IX propagation are also explored in GaN/AlGaN heterostructures with high E_{ex} reaching ~30 meV[18]. These low temperatures of operation limit the real world application of GaAs based excitonics.

Van der Waals heterostructures composed of atomically thin layers of Transition Metal Dichalcogenide (TMD) materials[19] allow the realization of excitons with high binding energies[20-21], in part due to the small IX spatial separation due to the atomically thin layer spacing. IXs in TMD heterostructures are characterized by binding energies reaching hundreds of meV[22-23] making them stable at room temperature[24]. Due to the high IX binding energy, TMD heterostructures can form a

material platform for creating excitonic devices operating at high temperatures suitable for real-world applications.

The majority of work on IXs in TMDs to date has been focused on the study of simple structures made of two different TMD layers[25-33], primarily $MoSe_2/WSe_2$ or MoS_2/WS_2 hetero-bilayers. Recent work has investigated IXs in more complex multilayer TMD structures such as bilayer WSe_2[34], bilayer $MoSe_2$[35], and trilayer $MoSe_2/WSe_2/MoSe_2$ structures[36]. These multilayer structures open the door to investigate more exotic phenomena such as IX droplet formation[37], and to serve as a well-suited platform to study IX attractive dipole forces[38].

The key to fabricating these multilayer devices is a quick and reliable method for determining the thickness, or more appropriately the layer number, of TMD flakes used in the fabrication process. One highly accurate method of thickness determination is atomic force microscopy (AFM), but this requires the TMD flakes to be subjected to forces that could potentially damage the flakes, and it also requires that the TMD materials are on a non-tacky substrate. In order to be measured they must be transferred, which relegates AFM to a layer verification role instead of a layer determination role.

Another non-destructive method that has been employed to determine layer thickness in TMD layers is Raman Spectroscopy[39]. This method has primarily been investigated for TMD flakes on Si/SiO_2 substrates, for which the thickness of the substrate significantly impacts the measurement. This method also requires a transfer step and similarly relegates Raman spectroscopy to a layer verification role instead of a layer determination role.

Optical contrast is a potential method that requires only a standard optical microscope and has been explored in few layer graphene on Si/SiO_2[40] and WS_2 on Si/SiO_2[41]. Both of these methods utilize color contrast of the flakes compared to their substrate in bright field images. This method shows promise, but is highly substrate dependent and again requires the TMD material to be already transferred.

Dark field optical microscopy provides another avenue to layer determination as utilizes greyscale images and for this reason could be more substrate tolerant. This method also places emphasis on the edges of materials, the point of focus for layer determination.

This work will utilize dark field optical contrast measurements of few-layer exfoliated TMD flakes on Si/SiO_2/PMGI/PMMA transfer ready substrates. This provides improved process integration of the layer determination step, allowing for quantitative layer determination to occur before any transfer. This will allow for quick and accurate selection of few-layer exfoliate TMD flakes in order to expedite the fabrication of structures to study indirect excitons and other excitonic devices. In order to calibrate the dark field optical measurements, AFM and low-temperature photoluminescence measurements are employed.

Chapter 2: Methodology

2.1 Fabrication

While there are many methods to fabricate TMD heterostructures, namely Chemical Vapor Deposition (CVD)[42], Molecular Beam Epitaxy (MBE)[43], and mechanical exfoliation[44], the highest quality samples used to study IXs to date have all been made with some variation of mechanical exfoliation and a dry transfer technique[45-46]. For this reason, the samples were assembled using a modified mechanical exfoliation and dry-transfer method[47].

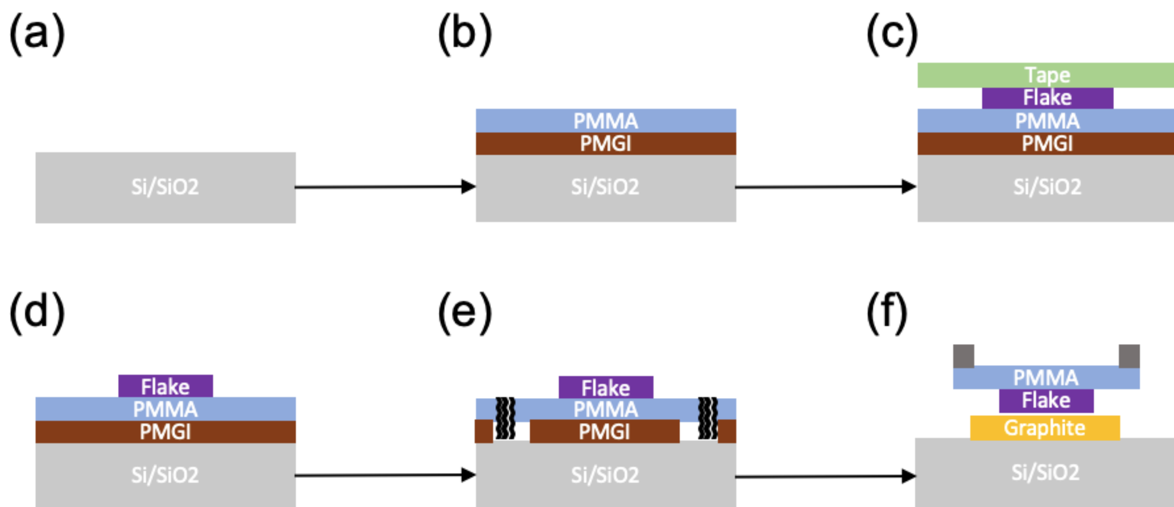

Figure 2. Fabrication process flow for dry-transfer technique. (a) bare Si/SiO_2 wafer (b) spin coated PMGI/PMMA (c) exfoliated TMD or h-BN flakes exfoliated using low-residue tape and pressed into heated PMMA (d) after cooling the tape is removed leaving the flakes on the PMMA surface (e) PMGI is undercut to free PMMA layer (f) PMMA layer holding the desired flake is transferred to a washer and subsequently transferred to a Si/SiO_2/Graphite substrate using a custom micro transfer stage.

Boron Doped Si wafers with 300nm of thermally grown SiO_2 were obtained and cleaned using IPA, Remover PG, an n-methyl 2-pyrrolidone (NMP) based solvent, and dried with N_2 gas. For the graphite back gates, the Si/SiO_2 wafers were subjected to a light plasma ashing step in Ar and O_2 gas to clean the surface from

and remaining contaminants and to expose hydrogen bonds to improve adhesion with the graphite. Separately, graphite flakes were exfoliated from bulk Highly Oriented Pyrolytic Graphite (HOPG) onto low-residue tape. Immediately following the ashing step, the tape holding the exfoliated graphite flakes was pressed into the Si/SiO_2 wafers and slowly peeled off. Once a graphite flake is selected the wafer is heated to 180°C for 20min to improve adhesion.

For the TMD and hexagonal-Boron Nitride (h-BN) layers, ~600nm of Polymethylgultarimide (PMGI) followed by ~150nm of Polymethyl Methacrylate (PMMA) were spun onto the Si/SiO2 wafers. Separately, TMD or h-BN flakes were exfoliated from bulk samples onto low-residue tape. The wafer is heated to 130°C to soften the PMMA and the tape containing the TMD or h-BN flakes is pressed into the PMMA and after allowing it to cool to room temperature, slowly peeled off. Desired TMD or h-BN flakes were selected via optical microscopy by a qualitative metric determined from previously obtained monolayer flakes based on contrast in both bright field and dark field images.

A circular cut is made through the PMMA layer and AZ 300 MIF Developer is added to dissolve the underlying PMGI layer, leaving a disc of free-standing PMMA with the desired TMD or h-BN flake in the center. This PMMA disc is floated onto DI water and transferred onto a washer coated with PMMA. The washer is attached to a three-axis micro-translation stage and lowered onto the desired substrate, heated to 80°C for transfer. Once the TMD or h-BN flake is deposited onto the substrate, the PMMA membrane is lifted off and discarded.

2.2 Optical Microscopy

The exfoliated graphite, h-BN, and TMD flakes are all imaged with both bright field and dark field optical microscopy using a Zeiss Axio Imager Optical Microscope with a 100x magnification objective.

Bright field imaging refers to the common imaging mode of collecting all light that passes through the sample into the objective. This allows for the acquisition of real color images for color contrast comparisons. Dark field imaging blocks out the light from the light source at the center of the optical axis, only allowing high angle light to pass through the sample. In this imaging scheme only the light which is diffracted, reflected or refracted by the sample to be collected by the objective. Because of this, darkfield imaging is well suited for imaging edges and interfaces.

2.3 AFM

AFM measurements were carried out in a VEECO Scanning Probe Microscope using a standard tapping mode procedure[48] with a vertical resolution of ~<1Å and lateral resolution of ~2nm. Tapping mode imaging was chosen to both maximize vertical resolution and minimize the risk of damage to the sample. Carbon coated Si tips with radius <20nm, cone angle of 40°, spring constant ~325kHz and force constant ~40N/m were used for all measurements.

2.4 Photoluminescence

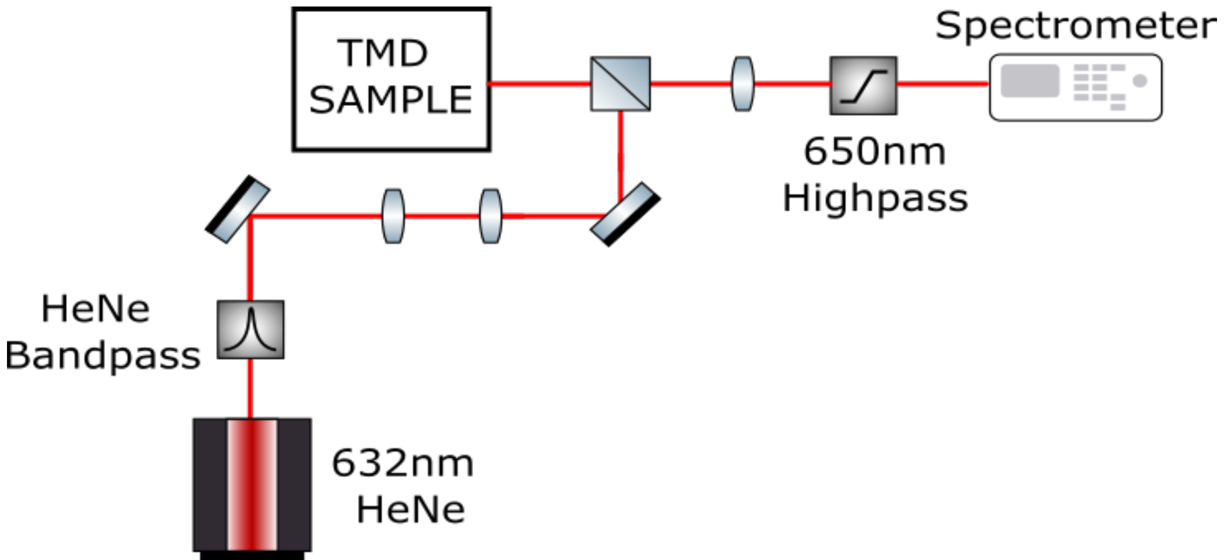

Figure 3. Optical setup for photoluminescence measurements. A multi-mode continuous wave HeNe laser is used to excite the sample in a cryostat with optically transparent quartz windows. A beamsplitter is used to collect the emitted light from the sample into a collection lens and through a 650nm highpass to remove any reflected laser light before being collected by a spectrometer. Measurements were taken at ~1.7K.

Photoluminescence measurements were carried out with the sample in a variable temperature 4He cryostat at ~1.7K. Flakes were excited using a continuous wave 632nm HeNe laser with excitation power between 50uW-3mW. The emitted light was passed through a 650nm highpass filter, below the energy of the laser but above the energy of any excitation, to exclude any reflected laser light from collected spectra. Spectra were collected using a spectrometer with a resolution of 0.2meV and a liquid nitrogen cooled Charge Coupled Device (CCD). The laser was defocused for sample defocused imaging and focused to a spot size of ~3um for spectral measurements.

Chapter 3: Results

The aim of this work is a facile method to determine layer thickness of TMD materials for sample fabrication of excitonic devices. Dark Field Optical Imaging of TMD flakes on Si/SiO_2/PMGI/PMMA was selected as it's the first step in the fabrication process, allowing for process integrated layer determination before any transfers are completed.

3.1 Optical Imaging

Exfoliation was carried out and a set of six flakes of $MoSe_2$ and eight flakes of WSe_2 were chosen for further study with optical microscopy. Both bright field and dark field images were captured at 100x magnification.

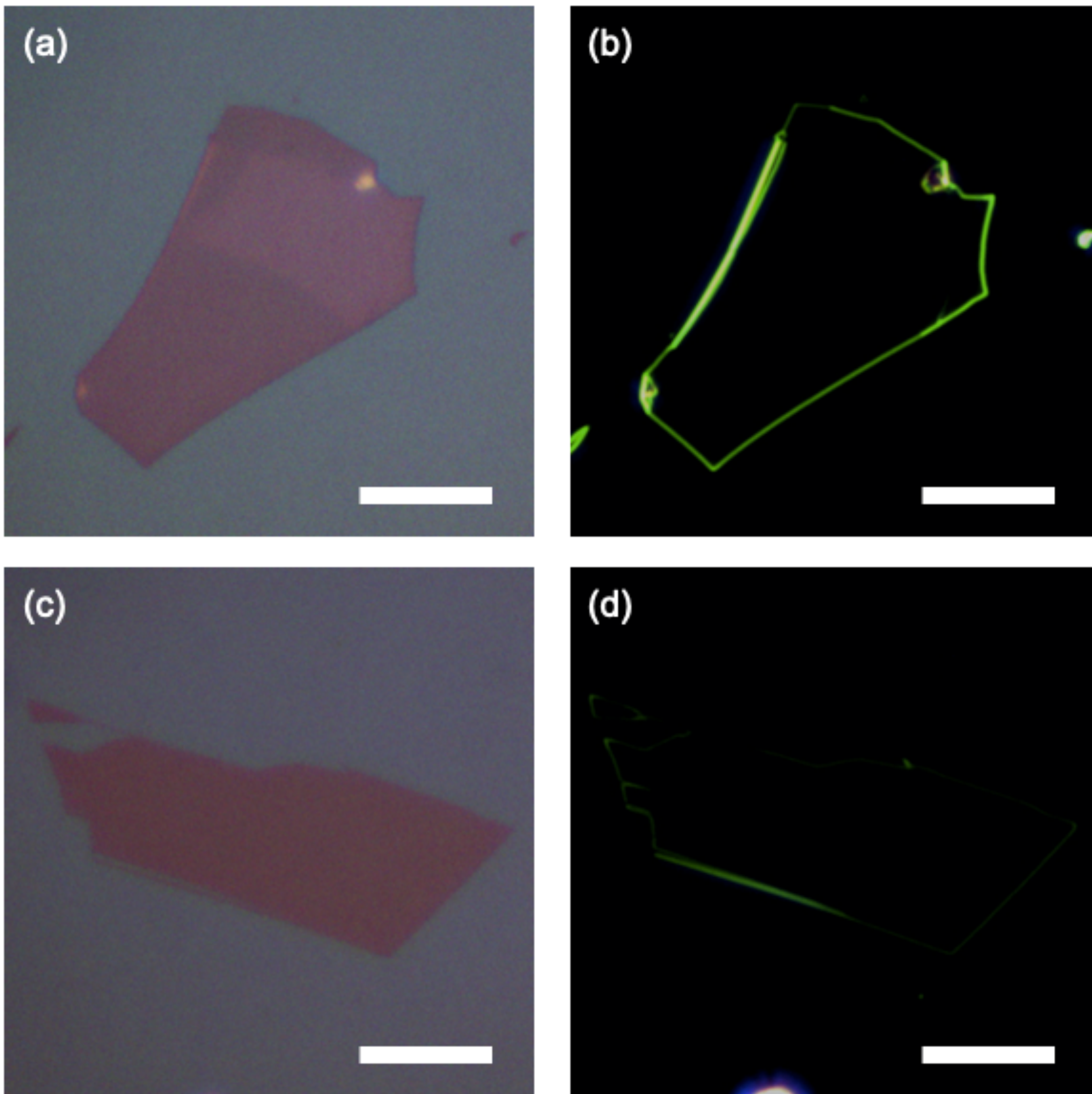

Figure 4. (a) Representative bright field image of $MoSe_2$ flake. Upper left hand corner is ML region. (b) the corresponding dark field image. (c) Representative bright field image of WSe_2 flake. Entire flake is monolayer. (d) the corresponding dark field image. All scale bars are 10µm. All images are taken through a 100x objective. Bright field images are taken with a 40s exposure time, dark field images were taken at 600s.

The contrast and intensity of the flake edge in the DF images were measured for all of these flakes. These measurements will be correlated with AFM and photoluminescence measurements to calibrate metrics in optical microscopy images to TMD flake layer number. A subset of three $MoSe_2$ flakes and three WSe_2 flakes

were selected to transfer onto graphite and h-BN to investigate further with AFM and photoluminescence measurements.

Although both bottom layer h-BN transfers were successful, each sample had a failed transfer. For the $MoSe_2$ sample a flake did not properly adhere to the bottom layer of h-BN and was lost, while for the WSe_2 sample a flake was folded and torn during transfer. The multiple transfer steps caused cracking and ripping in the flakes that were already transferred. This behavior was worse in the $MoSe_2$ sample, as seen by the cracking of the triangle flake and the tears and missing pieces from the large flake at the bottom of the sample. The WSe_2 sample suffered some tears in one of its flakes but it had the unintended benefit of revealing a bilayer region that was not seen in the optical images in the middle flake.

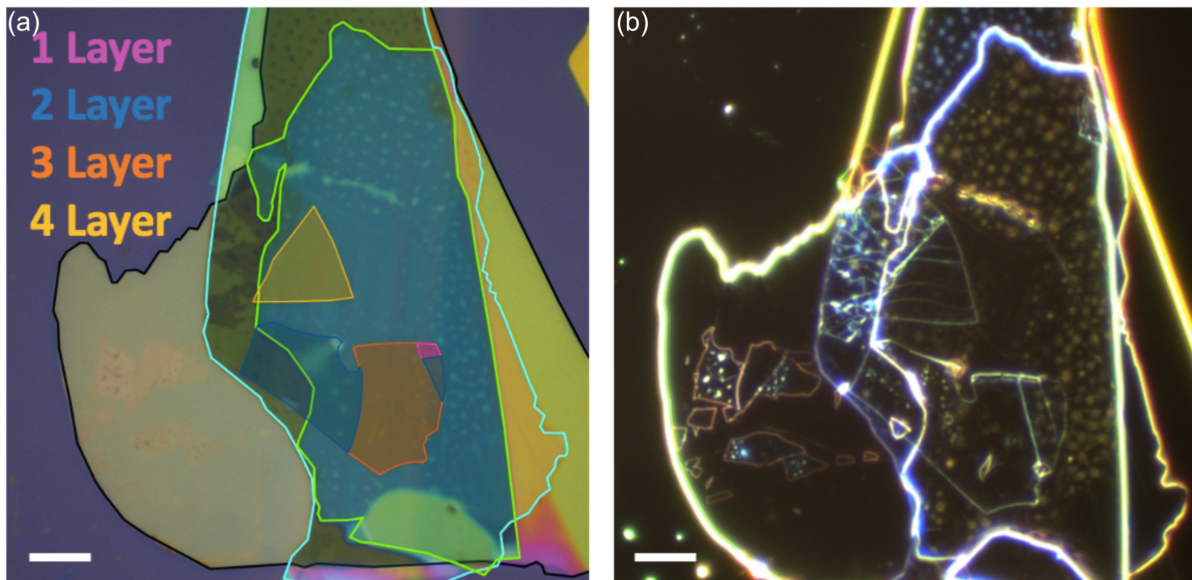

Figure 5. Optical microscope images showing (a) Bright field image of the $MoSe_2$ sample with areas of known layer number indicated with different colors. (b) Dark field image of the $MoSe_2$ sample. Both scale bars are 10μm. Both images are taken through a 100x objective. Bright field images are taken with a 40s exposure time, dark field images were taken at 600s.

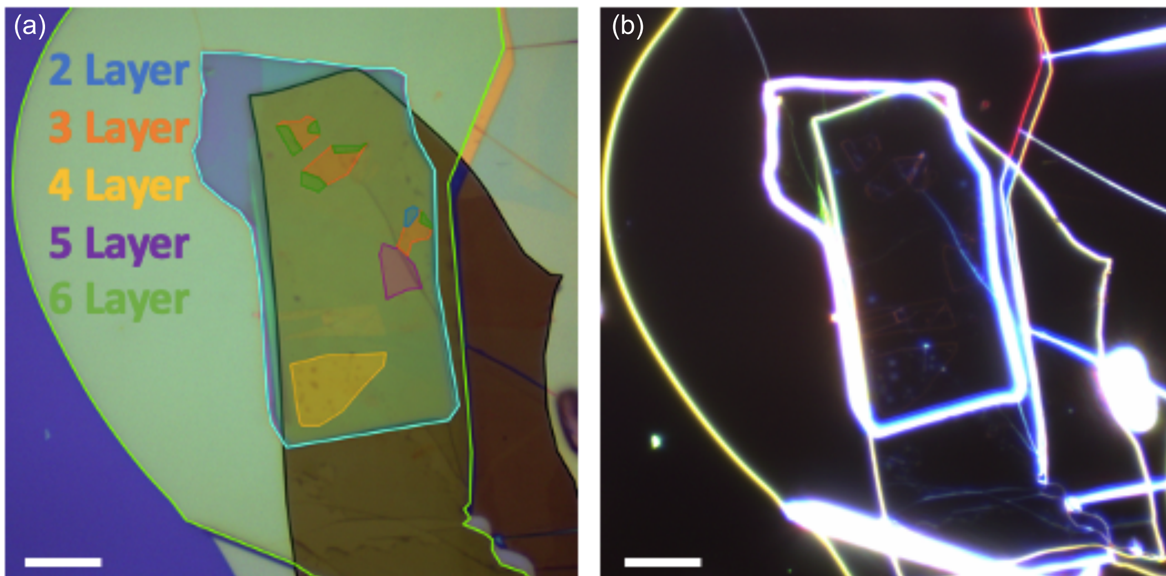

Figure 6. Optical microscope images showing (a) Bright field image of the WSe_2 sample with areas of known layer number indicated with different colors. The six layer regions are three layer regions folded onto themselves. (b) Dark field image of the WSe_2 sample. Both scale bars are 10μm. Both images are taken through a 100x objective. Bright field images are taken with a 40s exposure time, dark field images were taken at 600s.

3.2 AFM Measurements

AFM measurements of the transferred flakes both showed the damage from the transfer steps in detail. The bottom h-BN surface exhibits bubbling in both samples on the order of tens of nanometers, creating a non-smooth surface for the TMD flakes. The TMD flakes show a similar bubbling around the edges. The bottom h-BN layer in the $MoSe_2$ sample seems to be more heterogeneous. Cross-sections of the AFM images of multiple pixels wide and as long as possible were taken to determine the step heights of the flakes. Due to the significant heterogeneity of the samples, especially in the $MoSe_2$ sample's case, multiple cross-sections were averaged together to verify layer numbers.

The cross-sections of the $MoSe_2$ sample revealed monolayer, bilayer, trilayer, and four-layer regions with step heights of 1.150nm, 1.917nm, 2.534nm, and

3.401nm respectively. Similarly The cross-sections of the WSe_2 sample revealed bilayer, trilayer, four-layer, and five-layer regions with step heights of 2.150nm, 3.529nm, 4.694nm, and 5.145nm respectively. While the characteristic single layer thickness of $MoSe_2$ and WSe_2 is ~0.7nm[49] The AFM step heights measured here do not correspond exactly to integer values of the theoretical layer thickness as is common for AFM measurements of few-layer TMDs[50]. An offset factor to correct for this will be explored in Chapter 4.

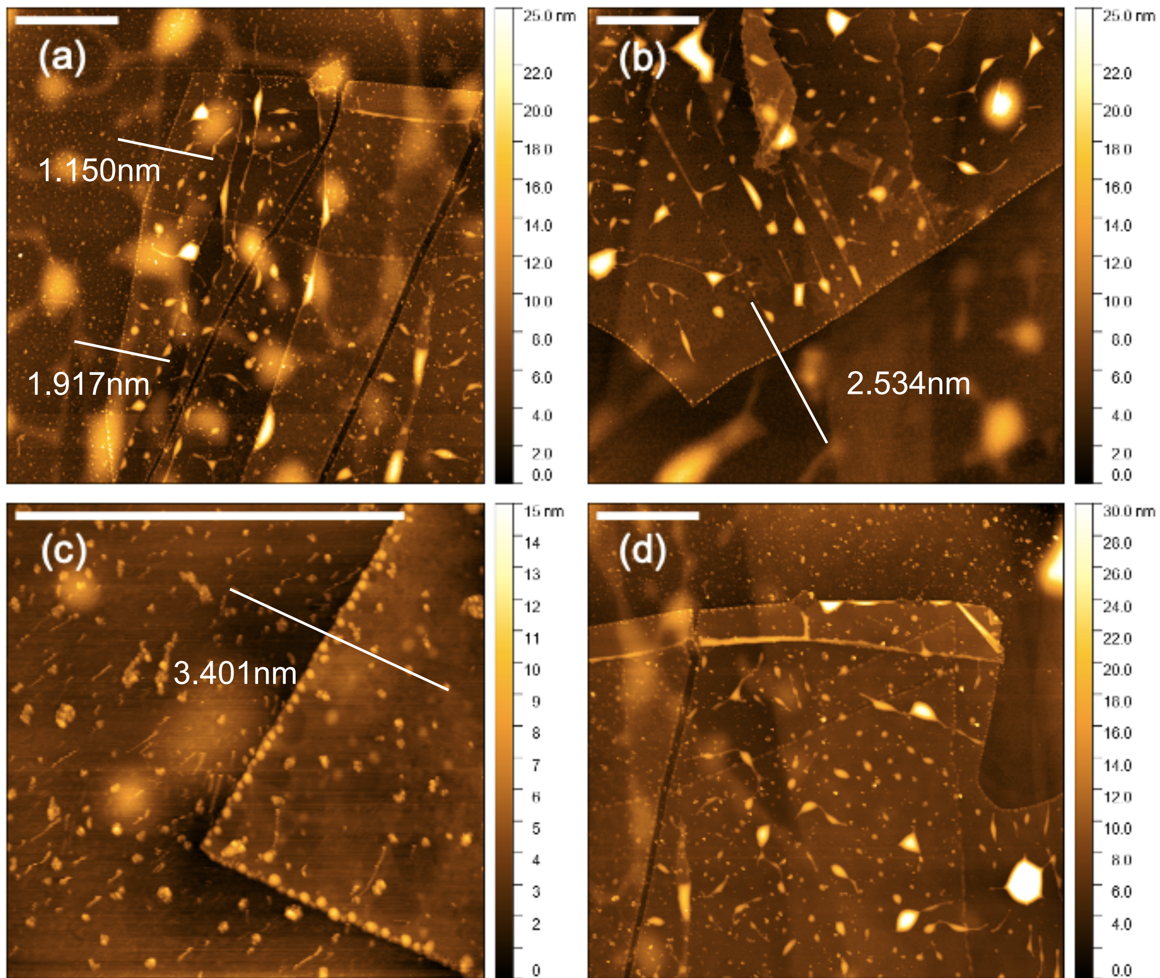

Figure 7. AFM images of $MoSe_2$ flakes transferred onto Si/SiO_2/Graphite/h-BN structure. Representative cross-sections shown as white bars. All scale bars are 2μm. (a) monolayer region, bilayer region, and bright spot (b) bilayer and trilayer regions (c) Four layer region at the tip of the triangle (d) bilayer and thicker regions.

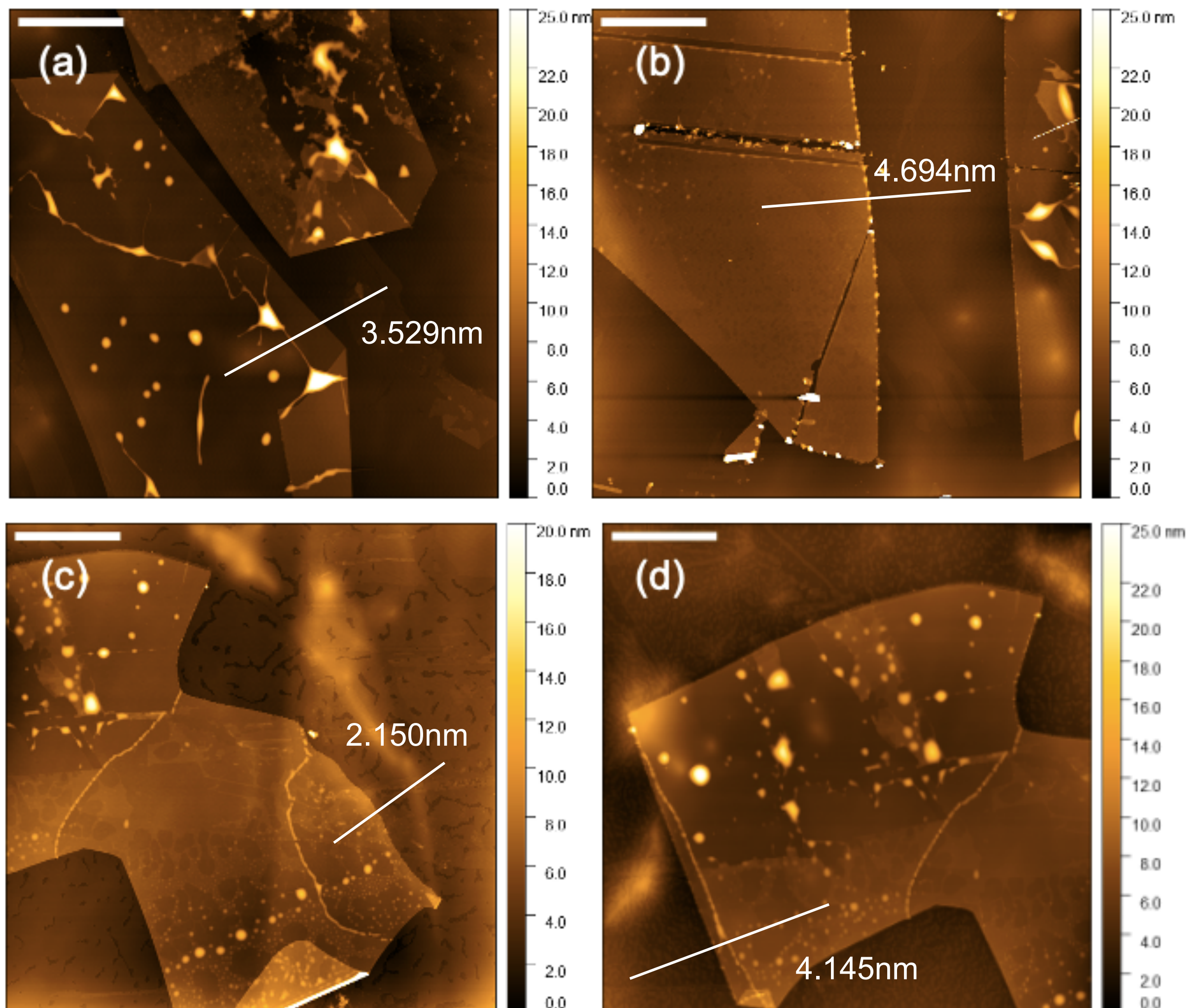

Figure 8. Tapping mode AFM images of WSe_2 flakes transferred onto Si/SiO_2/Graphite/h-BN structure. Representative cross-sections shown as white bars. All scale bars are 2μm. (a) trilayer region, (b) four-layer region, (c) four-layer, trilayer, and bilayer regions, (d) four-layer and five-layer regions.

3.3 Photoluminescence Measurements

Both defocused, broad-illumination images and photoluminescence spectra were captured for both samples. The broad-illumination images reveal weak signal, roughly two counts per second across the majority of both of the samples, which is expected for few-layer TMDs as their bandgap is indirect in momentum space[51]. The defocused image of the $MoSe_2$ sample shows clear bright spots which potentially

correspond to monolayer regions, as it is well-documented that monolayer emission in $MoSe_2$ is as much as 4000x stronger than in few-layer $MoSe_2$[52]. This points again to the heterogeneity of the sample. The bright spot labelled 1L BS doesn't correspond to any clear monolayer regions on the sample, but instead lies roughly in the same location as a tear through a bilayer region in the sample, which could have exposed a small monolayer region. The faint bright region labelled 1L corresponds to a 2x3μm monolayer region confirmed with AFM. The bright spot labelled 4L BS corresponds to the edge of the triangle flake, where no AFM images were taken. The optical DF images in this location potentially reveal a lifted edge or crack. The spot labelled 2L corresponds to a bilayer region confirmed with AFM.

3.3.1 $MoSe_2$ Photoluminescence Spectra

The 1 Layer Bright Spot region spectra shows two clear peaks at 1.625eV and 1.655eV with full width half max (FWHM) values of ~15meV. The lower energy peak also includes a low energy shoulder near 1.6eV. The energies of these peaks are in good agreement with the charged exciton or trion peak (T) and the ground state direct exciton peak (X) of $MoSe_2$ monolayers at cryogenic temperatures[45,53]. The relative intensity of this region is also ~250x the peak measured in the 2L spectra adding credence to the argument labelling this bright spot as a monolayer.

The 1 Layer region spectra interestingly only shows one broad peak (FWHM ~60meV) centered at a lower energy (1.605eV) than either of the peaks in the bright spot region. This could be a result of the tear through the center of the monolayer region, strain caused by a large (30nm and 18nm) bubbles present in the region

redshifting the trion peak[54], or some other unknown effect tied to the heterogeneity of the region.

The 4L Bright Spot region spectra shows many peaks across a wide spectral range of 1.52-1.67eV. The two highest energy peaks located at ~1.63eV and ~1.66eV could be attributed to the T and X peaks discussed earlier, with a blueshift of ~5meV. No significant monolayer material is expected in this area, so this could be due to some exposed monolayer at the edge of a lift or tear in the triangle flake. The relative intensity is 10x lower than the 1L Bright spot. The sharp lower energy peaks can potentially be assigned to defect states in the TMD material at the edge of the torn/lifted region as they are too low in energy to be assigned to X or T peaks and too high in energy to be assigned to indirect transitions in multilayer $MoSe_2$ which would be expected at even lower energies. This is explored further in section 3.3.3.

The 2L region spectra shows no emission higher than 1.6eV and only shows lower energy peaks at nearly the same location as the 4L BS spectra. These could be tied to the tear through the bilayer region or some unknown effect caused by the heterogeneity of the sample. No clearly identifiable peaks are visible in the spectrum from this region.

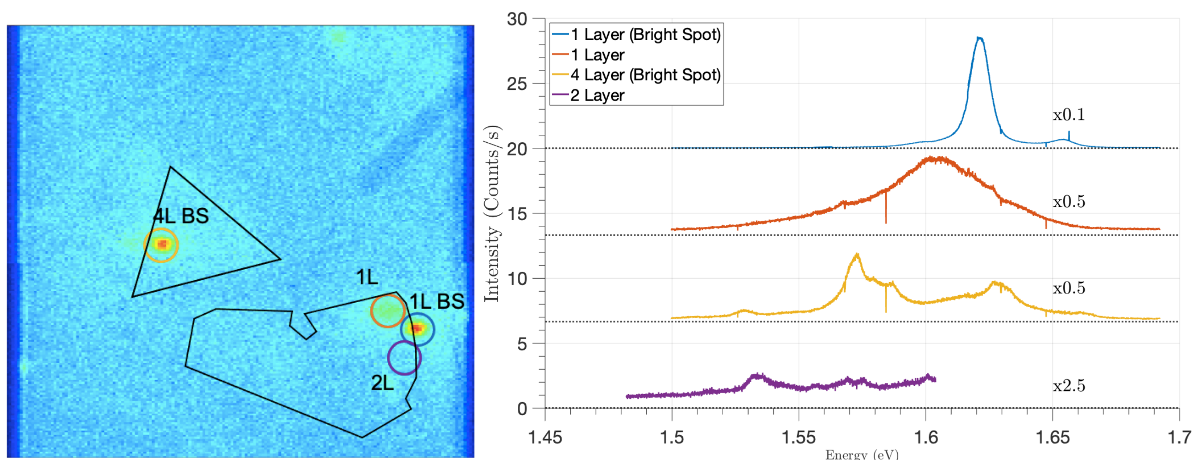

Figure 9. (a) Defocused illumination image of $MoSe_2$ sample. Laser spot size covers entire region of interest The circle markers are approximately the size of the excitation spot (3μm). (b) Spectra of regions labelled in the defocused image. Samples were excited at 632nm with an excitation power of 3mW at ~1.7K. Defocused image and spectra both taken with 300s exposure times through a 650nm highpass filter.

The weak signal from the majority of the sample, large amount of sample heterogeneity, and lack of clearly identifiable peaks in three out of four of the spectra make it unwise to heavily weight these photoluminescence measurements in the assignment of layer numbers to calibrate the dark field optical contrast measurements.

3.3.2 WSe_2 Photoluminescence Spectra

Although the defocused image of the WSe_2 sample again shows relatively weak emission across the sample, there are no bright spots, demonstrating the homogeneity of the transferred flakes. Each spot on the sample exhibited a high energy peak roughly at the same position ~1.7eV and a lower energy peak in the region ~1.3eV -1.55eV. A clear trend appears in the photoluminescence spectra: the lower energy peak shifts to lower energies monotonically with increasing layer

number. The intensity of the lower energy peak also seems to decrease monotonically with increasing layer number.

The 2L region spectra show two sections of peaks, one centered near 1.7eV and the other near 1.55eV. A third smaller peak is seen at ~1.4eV. The highest peak in the higher section of peaks (1.715eV) and the next lowest peaks (1.7eV, 1.6925eV) are in good agreement with the ground state neutral exciton (X) and the optically dark charged exciton[56] or trion (T) dublet peaks seen in photoluminescence spectra of monolayer and bilayer WSe_2 at cryogenic temperatures[45,52,56-57]. The lowest energy peak of the higher section of peaks could be explained as either a phonon sideband or another momentum-dark exciton. The lower section of peaks shows a dublet peak at 1.55eV and 1.542eV and a higher shoulder near 1.565eV, which could be explained as charged and neutral momentum-indirect excitons respectively. The lowest peak at 1.4eV corresponds to trilayer emission and is a result of the excitation spot slightly overlapping with a trilayer region confirmed with AFM.

The 3L region spectra again shows the trion peak but the lower energy dublet is not visible. Also missing are the neutral exciton peak and the ambiguous peak near 1.565eV. The lower energy section of peaks shows a trion peak again without a visible dublet, along with a higher energy shoulder that can be assigned to a trilayer trion peak.

The 4L region spectra shows a similar monolayer trion peak (1.695eV) along with a lower energy trion (1.32eV) and neutral exciton (1.33eV) peaks. The relative

intensity of all peaks also decreased by a factor of 2 compared to the bilayer and trilayer regions.

Continuing the trend the 5L region spectra shows a high energy peak corresponding to the monolayer trion (1.705eV) and a low energy peak corresponding to the five-layer trion (1.305eV). A five-layer neutral exciton peak is not visible, potentially because of the continued reduction of signal again by a factor of 2 compared to the four-layer region.

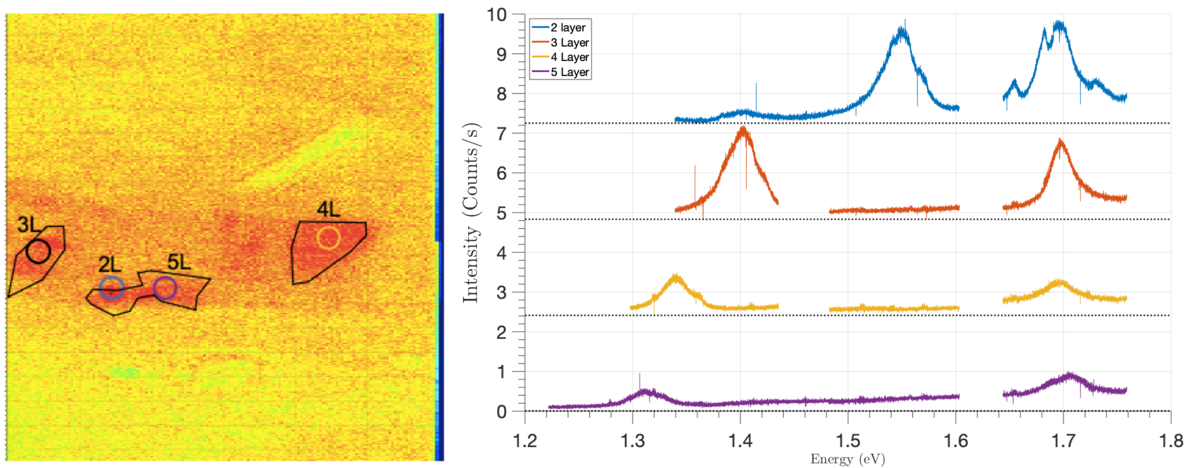

Figure 10. (a) Defocused illumination image of WSe_2 sample. Laser spot size covers entire region of interest The circle markers are approximately the size of the excitation spot (3μm). (b) Spectra of regions labelled in the defocused image. Samples were excited at 632nm with an excitation power of 3mW at ~1.7K. Defocused image and spectra both taken with 300s exposure times through a 650nm highpass filter.

The monotonically decreasing trend in the lower energy peaks provides an unambiguous metric for layer number, and when combined with AFM measurements creates a clear method for differentiating the layer number of WSe_2 flakes. Spectral lines from TMD samples are prone to variation on the order of 10meV, but as each redshift of the low energy peaks up to five-layers is greater than 10meV, the risk of misidentifying the layer number by peak position is low.

3.3.3 Photoluminescence Power Dependence and Crack/Edge Impact

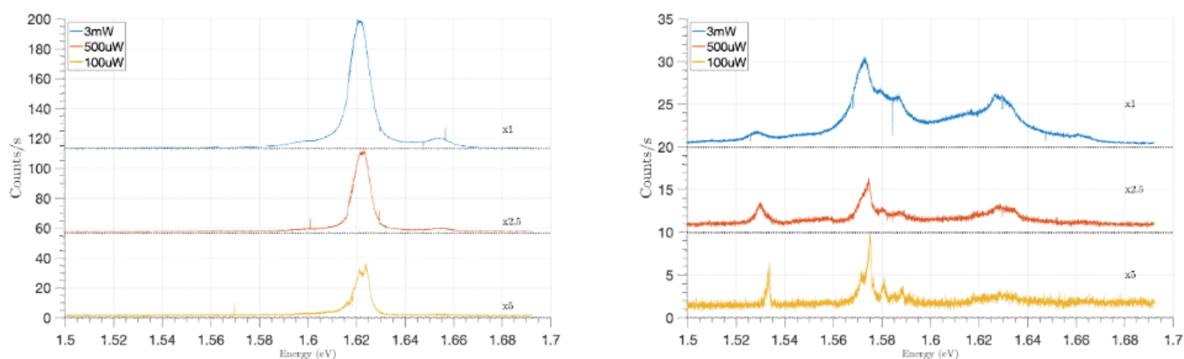

Figure 11. Power dependence of (a) $MoSe_2$ 1L bright spot and (b) 4L bright spot. Samples were excited at 632nm with an excitation powers from 3mW to 100μW at ~1.7K. Spectra taken with 300s exposure times through a 650nm highpass filter.

The excitation power dependence of the bright spots on the $MoSe_2$ sample were investigated to gain insight on the nature of the peaks. The relative intensity of the peaks decreased roughly by the same factor as the excitation power for the 1L bright spot, but in the 4L bright spot only the highest energy peak decreased by the same factor as the excitation power. A set of dublet peaks emerged in the monolayer trion peak in the 1L region at 500uW and became even more pronounced at 100uW. While the peak position and FWHM didn’t change by any appreciable amount in any of the peaks in the 1L bright spot region or in the highest peak in the 4L bright spot region, all the lower energy peaks in the 4L bright spot sample began to blueshift and narrow significantly. This anomalous narrowing potentially points towards assigning these peaks to defect states associated with edges, tears, or unintentional doping of the flake.

In an effort to better understand the high energy peak, spectra were measured at a region near edges/cracks and a region far from edges/cracks in the middle of a

flake. The four-layer flake was chosen as it had both large pristine regions far from edges and cracks and cracked regions near edges. While the relative intensity of the peaks remains roughly constant, a blueshift of ~15meV occurs at the region near cracks/edges. This shift is three times greater than the largest deviation from the neutral exciton peak position for any other flake on this sample, which along with the fact that both these spectra were collected from the same flake supports the idea that this isn't merely variation in peak position from flake to flake.

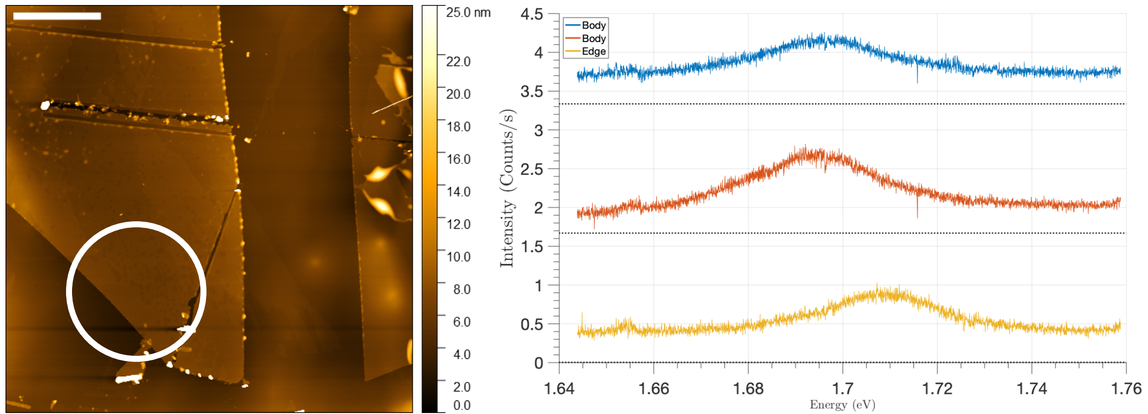

Figure 12. High energy peak shift when comparing region with a crack near an edge to two regions at the center of the flake far from edges or cracks. (a) AFM image of flake with edge excitation region shown, both body excitation regions are to the upper left of the image outside of the AFM field of view. Samples were excited at 632nm with an excitation power of 3mW at ~1.7K. Spectra taken with 300s exposure times through a 650nm highpass filter.

Chapter 4: Discussion

The ultimate goal of this work, utilizing only dark field microscope images to determine the layer number of $MoSe_2$ and WSe_2 flakes, requires a correlation of the dark field images to AFM and photoluminescence measurements.

Two different related values, the dark field intensity and the dark field contrast were measured. Cross sections were taken of flake edges and the greyscale pixel intensities were measured along the cross section and averaged across many cross sections over multiple edges of the flake (when possible). The dark field intensity is defined as the maximum peak value of the edge minus the background, while the dark field contrast is defined as the maximum peak value of the edge divided by the background.

The AFM step heights were subjected to a correction factor in the form of an offset and normalized to layer number by dividing by the thickness of a single layer. This provides a reasonable fit of the AFM data to integer values of layer number. There is a potential for a more accurate fit, such as using an offset that scales with the layer number, but this was avoided in this work as the sample sizes are small and due to this are at risk to “over-fitting” to reach ideal values.

4.1 $MoSe_2$ Calibration

The AFM step heights were fit using an offset of 0.45nm and a single layer thickness of 0.7nm. Both the dark field contrast and the dark field intensity increase roughly linearly with layer number. The dark field contrast seems to provide a more easily differentiable metric for layer number. One explanation for this that the flakes

of interest are rarely the only objects in the field of view of the microscope image, and in some cases nearby flakes or even large flakes far away scatter enough light to pollute the background of the image, which the dark field contrast corrects for more accurately.

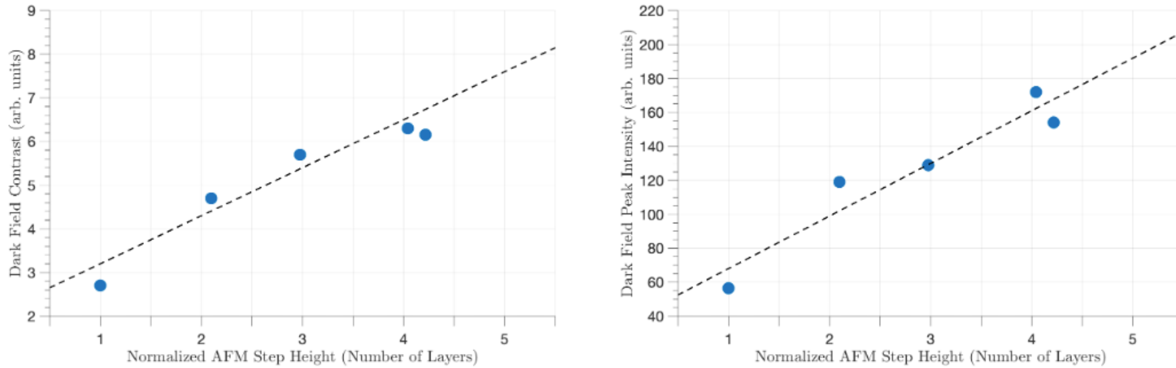

Figure 13. (a) Layer number (AFM step height - offset)/(monolayer thickness) of flakes on $MoSe_2$ sample versus the Dark field contrast: $(I-I_0)/I_0$ and (b) dark field peak intensity. I: dark field image peak intensity, I_0: dark field image background intensity. Dark field intensity values were measured on images captured using a 100x objective and factory default microscope settings with a 600s exposure time.

4.2 WSe_2 Calibration

The clear trend of the lower energy peaks redshifting with increasing layer number can be used in addition to AFM as another indicator of layer number. The AFM step heights were fit using an offset of 0.9nm and a single layer thickness of 0.65nm.

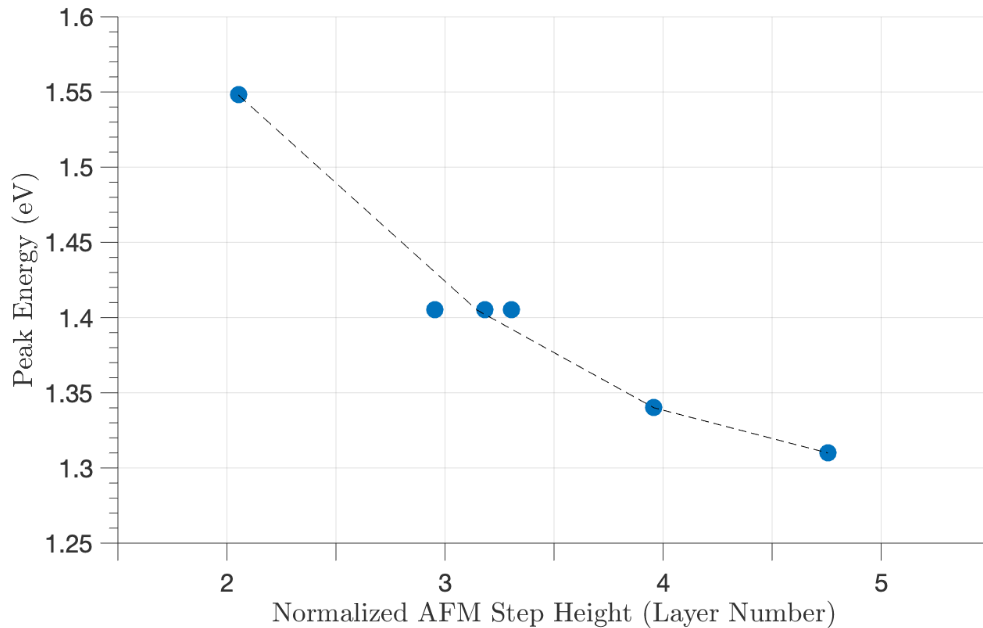

Figure 14. Peak energy by layer number (AFM step height - offset)/(monolayer thickness) for the WSe_2 sample. The low energy peak position shifts monotonically with increasing layer number. The set of three points around 3 layers are from three different flakes, demonstrating the moderate level of variation in AFM step heights in comparison to the minimal variation in peak location.

One can also compare the trion peak position of our sample to other experimental results. The most significant variation appears in the monolayer trion energy, varying over 50meV. Our work shows very close agreement with previous experimental results for monolayer and bilayer WSe_2[59-61], and is also in agreement with previous work on trilayer and four-layer flakes[62]. The main deviation occurs with

the sole CVD grown flake shown for comparison[63], which can be expected for CVD grown flakes as they generally have higher defect densities than exfoliated samples.

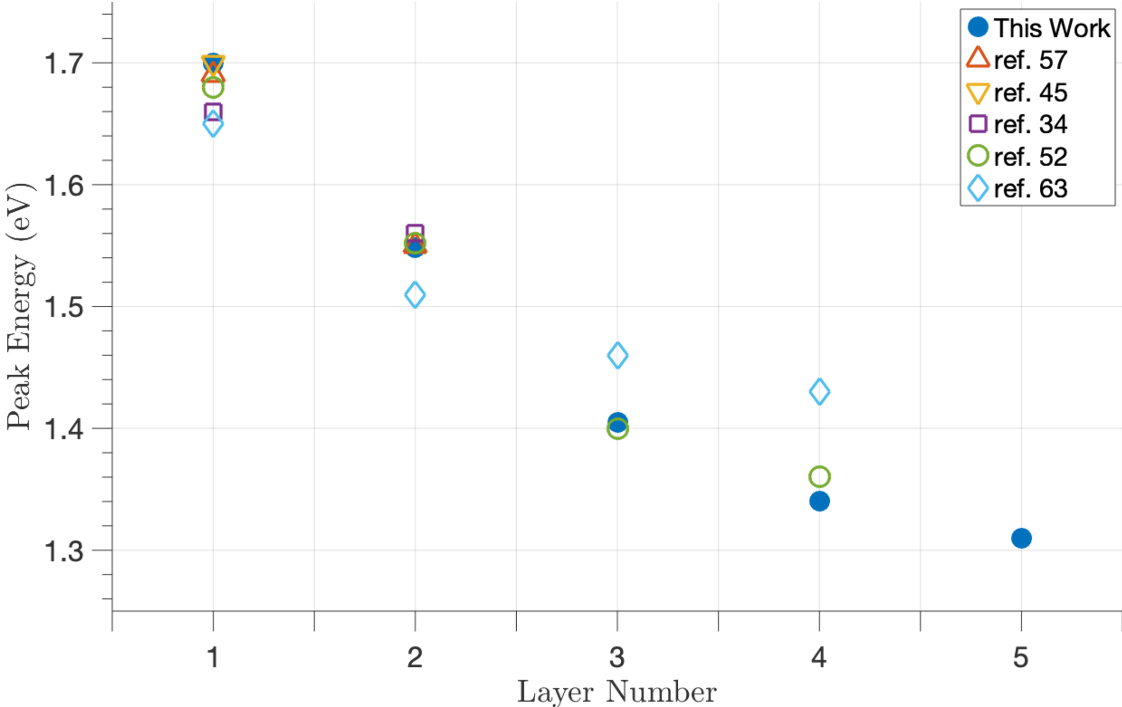

Figure 15. Comparison to measured peak positions by layer number in the literature is in good agreement with this work. As no pristine monolayer region exists on this sample, the 1L peak from this work is the average energy of the high energy peak at each location on the sample.

Similarly to the $MoSe_2$ sample, both the dark field contrast and the dark field intensity increase roughly linearly with layer number. Again the dark field contrast seems to provide a more easily differentiable metric for layer number, although less clearly. No bilayer regions were measured using dark field imaging as the bilayer region measured by AFM and photoluminescence measurements only appeared as a result of damage to the flake during the transfer process.

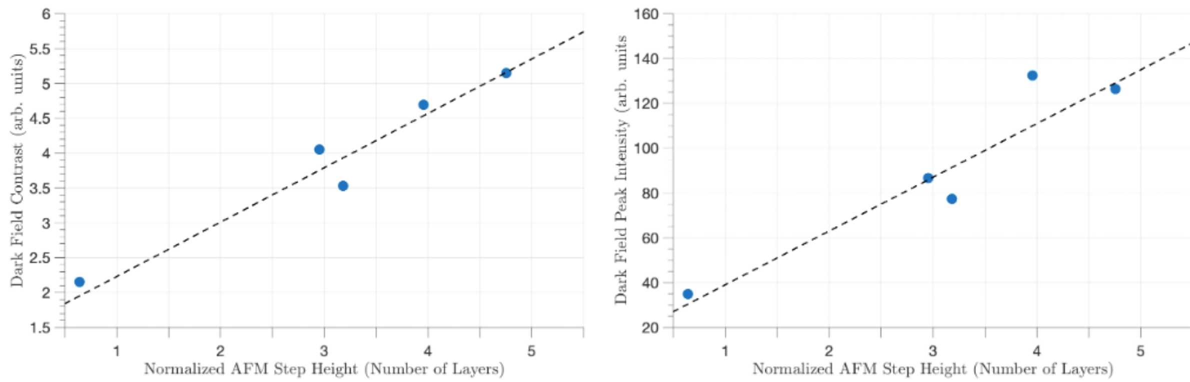

Figure 16. (a) Layer number (AFM step height - offset)/(monolayer thickness) of flakes on WSe_2 sample versus the Dark field contrast: $(I-I_0)/I_0$ and (b) dark field peak intensity. I: dark field image peak intensity, I_0: dark field image background intensity. Dark field intensity values were measured on images captured using a 100x objective and factory default microscope settings with a 600s exposure time.

Chapter 5: Summary and Recommendations for Further Work

This work has established dark field microscopy as a suitable fabrication process-integrated method for layer determination in few-layer exfoliated $MoSe_2$ and WSe_2. TMD flakes were exfoliated onto substrates that would be used for transfer and imaged. After transfer, they were investigated using AFM and photoluminescence to accurately determine the layer number of the flake. The heterogeneity of the $MoSe_2$ sample limited the efficacy of photoluminescence measurements, while the photoluminescence measurements of the WSe_2 were used to bolster the AFM measurements. Power dependence of various regions on both samples were investigated along with the impact that edges/cracks might have on the spectra.

The contrast and intensity of flake edges in dark field microscope images were correlated to AFM and photoluminescence measurements. Not only does this allow for more accurate layer determination, it also provides a growing framework that additional data points can be added to as more flakes are exfoliated and devices are fabricated to passively improve the fit.

Investigation into the impact of PMGI/PMMA thickness, spectra captured at the edge of a flake vs. the center, and expansion to other TMD materials such as MoS_2, WS_2 that provide an interesting platform to study indirect excitons are all next step expansions of this work.

This facile layer determination method can also be used to facilitate the fabrication of more complex structures to probe dipolar interaction between separated indirect excitons in double hetero-bilayer device or to investigate indirect excitons in trilayer $MoSe_2$ and WSe_2 and beyond.

References

1. This introduction closely follows a previous work from this lab, cited in ref. 45.

2. Y.E. Lozovik, V.I. Yudson, A new mechanism for superconductivity: pairing between spatially separated electrons and holes, Sov. Phys. JETP 44, 389 (1976).

3. M. Hagn, A. Zrenner, G. Bohm, G. Weimann, Electric field-induced exciton transport in coupled quantum well structures, Appl. Phys. Lett. 67, 232 (1995).

4. A. Gartner, A.W. Holleitner, J.P. Kotthaus, D. Schuh, Drift mobility of long-living excitons in coupled GaAs quantum wells, Appl. Phys. Lett. 89, 052108 (2006).

5. S. Zimmermann, G. Schedelbeck, A.O. Govorov, A. Wixforth, J.P. Kotthaus, M. Bichler, W. Wegscheider, G. Abstreiter, Spatially resolved exciton trapping in a voltage controlled lateral superlattice, Appl. Phys. Lett. 73, 154 (1998) .

6. M. Remeika, J.C. Graves, A.T. Hammack, A.D. Meyertholen, M.M. Fogler, L.V. Butov, M. Hanson and A.C. Gossard, Localization-Delocalization Transition of Indirect Excitons in Lateral Electrostatic Lattices, Phys. Rev. Lett. 102, 186803 (2009).

7. M. Remeika, M.M. Fogler, L.V. Butov, M. Hanson, A.C. Gossard, Two-Dimensional Electrostatic Lattices for Indirect Excitons, Appl. Phys. Lett. 100, 061103 (2012).

8. X.P. Vogele, D. Schuh, W. Wegscheider, J.P. Kotthaus, A.W. Holleitner, Density Enhanced Diffusion of Dipolar Excitons within a One-Dimensional Channel, Phys. Rev. Lett. 103, 126402 (2009).

9. K. Cohen, R. Rapaport, P.V. Santos, Remote Dipolar Interactions for Objective Density Calibration and Flow Control of Excitonic Fluids, Phys. Rev. Lett. 106, 126402 (2011).

10. A.G. Winbow, J.R. Leonard, M. Remeika, Y.Y. Kuznetsova, A.A. High, A.T. Hammack, L.V. Butov, J. Wilkes, A.A. Guenther, A.L. Ivanov, M. Hanson, A.C. Gossard, Electrostatic Conveyer for Excitons, Phys. Rev. Lett. 106, 196806 (2011).

11. C.J. Dorow, J.R. Leonard, M.M. Fogler, L.V. Butov, K.W. West, L.N. Pfeiffer, Split-gate device for indirect excitons, Appl. Phys. Lett. 112, 183501 (2018).

12. C.J. Dorow, M.W. Hasling, D.J. Choksy, J.R. Leonard, L.V. Butov, K.W. West, L.N. Pfeiffer, High-mobility indirect excitons in wide single quantum well, Appl. Phys. Lett. 113, 212102 (2018).

13. A.A. High, E.E. Novitskaya, L.V. Butov, M. Hanson, A.C. Gossard, Control of exciton fluxes in an excitonic integrated circuit, Science 321, 229 (2008).

14. G. Grosso, J. Graves, A.T. Hammack, A.A. High, L.V. Butov, M. Hanson, A.C. Gossard, Excitonic switches operating at around 100 K, Nature Photonics 3, 577-580 (2009).

15. D.S. Chemla, D.A.B. Miller, P.W. Smith, A.C. Gossard, W. Wiegmann, Room temperature excitonic nonlinear absorption and refraction in GaAs/AlGaAs multiple quantum well structures, IEEE J. Quantum Electron. 20, 265-275 (1984).

16. K. Sivalertporn, L. Mouchliadis, A.L. Ivanov, R. Philp, E.A. Muljarov, Direct and indirect excitons in semiconductor coupled quantum wells in an applied electric field, Phys. Rev. B 85, 045207 (2012).

17. A. Zrenner, P. Leeb, J. Schafler, G. Bohm, G. Weimann, J.M. Worlock, L.T. Florez, J.P. Harbison, Indirect excitons in coupled quantum well structures, Surf. Sci. 263, 496-501 (1992).

18. Francois Chiaruttini, Thierry Guillet, Christelle Brimont, Benoit Jouault, Pierre Lefebvre, Jessica Vives, Sebastien Chenot, Yvon Cordier, Benjamin Damilano, Maria Vladimirova, Trapping Dipolar Exciton Fluids in GaN/(AlGa)N Nanostructures, Nano Lett. 19, 4911-4918 (2019).

19. A.K. Geim, I.V. Grigorieva, Van der Waals heterostructures, Nature 499, 419-425 (2013).

20. Ziliang Ye, Ting Cao, Kevin O'Brien, Hanyu Zhu, Xiaobo Yin, Yuan Wang, Steven G. Louie, Xiang Zhang, Probing excitonic dark states in single-layer tungsten disulphide, Nature 513, 214-218 (2014).

21. Alexey Chernikov, Timothy C. Berkelbach, Heather M. Hill, Albert Rigosi, Yilei Li, Ozgur Burak Aslan, David R. Reichman, Mark S. Hybertsen, Tony F. Heinz, Exciton Binding Energy and Nonhydrogenic Rydberg Series in Monolayer WS2, Phys. Rev. Lett. 113, 076802 (2014).

22. M.M. Fogler, L.V. Butov, K.S. Novoselov, Hightemperature superfluidity with indirect excitons in van derWaals heterostructures, Nature Commun. 5, 4555 (2014).

23. Thorsten Deilmann, Kristian Sommer Thygesen, Interlayer Trions in the MoS_2/WS_2 van der Waals Heterostructure, Nano Lett. 18, 1460 (2018).

24. E.V. Calman, M.M. Fogler, L.V. Butov, S. Hu, A. Mishchenko, A.K. Geim, Indirect excitons in van der Waals heterostructures at room temperature, Nature Commun. 9, 1895 (2018).

25. Schaibley, J., Yu, H., Clark, G., Rivera, P., Ross, J.S., Seyler, K.L., Yao, W., Xu, X. Valleytronics in 2D materials. Nat Rev Mater 1, 16055 (2016).

26. Rivera, P., Seyler, K.L., Yu, H., Schaibley, J.R..Yan, J., Mandrus, D.G., Yao, W., Xu, X. Valley-polarized exciton dynamics in a 2D semiconductor heterostructure. *Science* 351, 6274 (2016).

27. Hong, X., Kim, J., Shi, S.-F., Zhang, Y., Jin, C., Sun, Y., Tongay, S., Wu, J., Zhang, Y., Wang, F. Ultrafast charge transfer in atomically thin MoS2/WS2 heterostructures. Nat. Nanotechnol. 9, (9), 682-686. (2014).

28. Ceballos, F.; Ju, M.-G.; Lane, S. D.; Zeng, X. C.; Zhao, H. Highly Efficient and Anomalous Charge Transfer in van der Waals Trilayer Semiconductors. Nano Lett. 17, (3), 1623-1628. (2017).

29. Rivera, P.; Schaibley, J. R.; Jones, A. M.; Ross, J. S.; Wu, S.; Aivazian, G.; Klement, P .; Seyler, K.; Clark, G.; Ghimire, N. J.; Y an, J.; Mandrus, D. G.; Y ao, W .; Xu, X. Observation of long-lived interlayer excitons in monolayer MoSe2–WSe2 heterostructures. Nat. Commun. 6, 6242. (2015).

30. Kim, J.; Jin, C.; Chen, B.; Cai, H.; Zhao, T.; Lee, P.; Kahn, S.; Watanabe, K.; Taniguchi, T.; Tongay, S.; Crommie, M. F.; Wang, F. Observation of ultralong valley lifetime in WSe2/MoS2 heterostructures. Science Advances 3, 7 (2017).

31. Lee, C.H., Lee, G.H., van der Zande, A. M., Chen, W., Li, Y., Han, M., Cui, X., Arefe, G., Nuckolls, C., Heinz, T. F., Guo, J., Hone, J., Kim, P. Atomically thin p–n junctions with van der Waals heterointerfaces. Nature Nanotech 9, 676–681 (2014).

32. Wilson, N. R.; Nguyen, P. V.; Seyler, K.; Rivera, P.; Marsden, A. J.; Laker, Z. P. L.; Constantinescu, G. C.; Kandyba, V.; Barinov, A.; Hine, N. D. M.; Xu, X.; Cobden, D. H. Determination of band offsets, hybridization, and exciton binding in 2D semiconductor heterostructures. Sci. Adv. 3, (2). (2017).

33. Zhang, C.; Chuu, C.-P .; Ren, X.; Li, M.-Y .; Li, L.-J.; Jin, C.; Chou, M.-Y .; Shih, C.-K. Interlayer couplings, Moiré patterns, and 2D electronic superlattices in MoS2/WSe2 hetero-bilayers. Sci. Adv. 3, (1), (2017).

34. Wang, Z., Chiu, Y.H., Honz, K., Mak, K.F., Shan, J., Electrical Tuning of Interlayer Exciton Gases in WSe2 Bilayers *Nano Letters*, *18* (1), 137-143 (2018).

35. Marcellina, E., Liu, X., Hu, X., Fieramosca, A., Huang, Y., Du, W., Liu, S., Zhao, J., Watanabe, K., Taniguchi, T., Xiong Q., Evidence for Moiré Trions in Twisted $MoSe_2$ Homobilayers. *Nano* Letters 21 (10), 4461-4468 (2021).

36. Choi, C., Huang, J., Cheng, HC., Kim, H., Vinod, A.K., Bae, S.H., Ozcelik, V.O., Grassi, R., Chae, J., Huang, S.W., D, X., Kaasbjerg, K., Low, T., Wong, C.W. Enhanced interlayer neutral excitons and trions in trilayer van der Waals heterostructures. npj 2D Mater Appl 2, 30 (2018).

37. M. Sammon, M., Shklovskii, B.I. Attraction of indirect excitons in van der Waals heterostructures with three semiconducting layers. Phys. Rev. B 99, 165403 (2019).

38. Choksy, D.J., Xu, C., Fogler, M.M., Butov, L.V., Norman, J., Gossard, A.C., Attractive and repulsive dipolar interaction in bilayers of indirect excitons. Phys. Rev. B 103, 045126 (2021).

39. Li, X.L., Qiao, X.F., Han, W.P., Zhang, X., Tan, Q.H., Chen, T., Tan, P.H. Determining layer number of two-dimensional flakes of transition-metal dichalcogenides by the Raman intensity from substrates. Nanotechnology 27 145704 (2016).

40. Bayle, M., Reckinger, N., Felten, A., Landois, P., Lancry, O., Dutertre, B., Colomer, J.F., Zahab, A.A., Henrard, L., Sauvajol, J.L., and Paillet, M. Determining the number of layers in few-layer graphene by combining Raman spectroscopy and optical contrast. J. Raman Spectrosc., 49: 36– 45 (2018).

41. Hu, X., Qiu, C. & Liu, D. Rapid thin-layer WS_2 detection based on monochromatic illumination photographs. Nano Res. 14, 840–845 (2021).

42. Zhang, Y., Yao, Y., Sendeku, M. G., Yin, L., Zhan, X., Wang, F., Wang, Z., He, J., Recent Progress in CVD Growth of 2D Transition Metal Dichalcogenides and Related Heterostructures. *Adv. Mater.*, 31, 1901694. (2019).

43. Choudhury, T.H., Zhang, X., Al Balushi, Z.Y., Chubarov, M., Redwing, J.M. Epitaxial Growth of Two-Dimensional Layered Transition Metal Dichalcogenides. Annual Review of Materials Research 50:1, 155-177 (2020).

44. Radisavljevic, B., Radenovic, A., Brivio, J., Giacometti, V., Kis, A. Single-layer MoS_2 transistors. Nature Nanotech 6, 147–150 (2011).

45. Calman, E.V., Fowler-Gerace, L.H., Choksy, D.J., Butov, L.V., Nikonov, D.E., Young, I.A., Hu, S., Mishchenko, A., Geim A.K. Indirect Excitons and Trions in $MoSe_2/WSe_2$ van der Waals Heterostructures. *Nano Letters 20* (3), 1869-1875 (2020).

46. Liu, E., Barré, E., van Baren, J., Wilson, M., Taniguchi, T., Watanabe, K., Cui, Y.T., Gabor, N.M., Heinz, T.F., Chang, Y.C., Lui, C.H. Signatures of moiré trions in $WSe_2/MoSe_2$ heterobilayers. Nature 594, 46–50 (2021).

47. Withers, F., Pozo-Zamudio, O.D., Mishchenko, A., Rooney, A.P., Gholinia, A., Watanabe, K., Taniguchi, T., Haigh, S.J., Geim, A.K., Tartakovskii, A.I., Novoselov. K.S. Light-emitting diodes by band-structure engineering in van der Waals heterostructures, Nature Materials 14, 301-306 (2015).

48. SPM Training Notebook, 3rd ed., Veeco Instruments Inc., Plainview, NY, USA (2003).

49. Tongay, S., Suh, J., Ataca, C., Fan, W., Luce, A., Kang, J.S., Liu, J., Ko, C., Raghunathanan, R., Zhou, J., Ogletree, F., Li, J., Grossman J.C., Wu, J. Defects activated photoluminescence in two-dimensional semiconductors: interplay between bound, charged and free excitons. Sci Rep 3, 2657 (2013).

50. Godin, K., Cupo, C., Yang, EH. Reduction in Step Height Variation and Correcting Contrast Inversion in Dynamic AFM of WS2 Monolayers. Sci Rep 7, 17798 (2017).

51. Mak, K., Shan, J. Photonics and optoelectronics of 2D semiconductor transition metal dichalcogenides. Nature Photon 10, 216–226 (2016).

52. Arora, A., Koperski, M., Nogajewski, K., Marcus, J., Faugeras, C., Potemski, M. Excitonic resonances in thin films of WSe2: from monolayer to bulk material Nanoscale,7, 10421-10429 (2015).

53. Calman, E.V., Fowler-Gerace, L.H., Choksy, D.J., Butov, L.V., Nikonov, D.E., Young, I.A., Hu, S., Mishchenko, A., Geim A.K. Indirect Excitons and Trions in $MoSe_2/WSe_2$ van der Waals Heterostructures. Nano Letters 20 (3), 1869-1875 (2020).

54. Arora, A., Nogajewski, K., Molas, M., Koperski, M., Potemski, M. Exciton band structure in layered $MoSe_2$: From monolayer to bulk limit. Nanoscale, 7, 20769-20775 (2015).

55. Ji, J., Zhang, A., Xia, T., Gao, P., Jie, Y., Zhang, Q., Zhang., Q. Strain-modulated excitonic gaps in mono- and bi-layer $MoSe_2$. *Chinese Phys. B* 25 077802 (2016).

56. Zhang, X.X., You, Y., Zhao, S.Y.F., Heinz, T.F. Experimental Evidence for Dark Excitons in Monolayer WSe_2. Phys. Rev. Lett. 115, 257403 (2015).

57. Förste, J., Tepliakov, N.V., Kruchinin, S.Y., Lindlau, J., Funk, V., Förg, M., Watanabe, K., Taniguchi, T., Baimuratov, A.S., Högele, A. Exciton g-factors in monolayer and bilayer WSe_2 from experiment and theory. Nat Commun 11, 4539 (2020).

58. Łopion, A., Goryca, M., Smolenski, T., Oreszczuk, K., Nogajewski, K., Molas, M.R., Potemski, M., Kossacki, P. Temperature dependence of photoluminescence lifetime of atomically-thin WSe_2 layer. *Nanotechnology* 31 135002 (2020).

59. Förste, J., Tepliakov, N.V., Kruchinin, S.Y., Lindlau, J., Funk, V., Förg, M., Watanabe, K., Taniguchi, T., Baimuratov, A.S., Högele, A. Exciton g-factors in monolayer and bilayer WSe_2 from experiment and theory. Nat Commun 11, 4539 (2020).

60. Calman, E.V., Fowler-Gerace, L.H., Choksy, D.J., Butov, L.V., Nikonov, D.E., Young, I.A., Hu, S., Mishchenko, A., Geim A.K. Indirect Excitons and Trions in $MoSe_2/WSe_2$ van der Waals Heterostructures. *Nano Letters 20* (3), 1869-1875 (2020).

61. Wang, Z., Chiu, Y.H., Honz, K., Mak, K.F., Shan, J. Electrical Tuning of Interlayer Exciton Gases in WSe2 Bilayers. Nano Lett. 18, 1, 137–143 (2018).

62. Arora, A., Koperski, M., Nogajewski, K., Marcus, J., Faugeras, C., Potemski, M. Excitonic resonances in thin films of WSe2: from monolayer to bulk material Nanoscale,7, 10421-10429 (2015).

63. Xu, K., Wang, Z., Du, X., Safdar, M., Jiang, C., He, J. Atomic-layer triangular WSe2 sheets: synthesis and layer-dependent photoluminescence property. *Nanotechnology* 24 465705 (2013).

Appendix 1: MATLAB Script for Dark Field Image Processing

```
%% ML DF Intensity
% Jeff Patz
% June 2021
%% MoSe Initialize

MoSe = {rgb2gray(imread('Mo_ZW1_ML.jpg')),...
    rgb2gray(imread('Mo_ZW2_ML.jpg')),...
    rgb2gray(imread('Mo_JP1_4.jpg')),...
    rgb2gray(imread('Mo_JP2_Multi.jpg')),...
    rgb2gray(imread('Mo_JP3_ML.jpg')),...
    rgb2gray(imread('Mo_JP4_ML.jpg'))};

%% MoSe Individual thetas, locations, and slices
Mo_DF_Contrast = [];
Mo_Contrast_err = [];
Mo_DF_Intensity = [];
Mo_Intensity_err = [];
MoSe_th = [];
temp = [];

th_1 = [55,43,28,-20];

loc_1 = [750,1750,750,1750;...
    750,1750,750,1750;...
    650,1650,750,1750;...
    750,1750,750,1750];

sl_1 = [550,650,400,500;...
    450,550,750,800;...
    600,700,650,750;...
    560,630,590,630;];

th_2 = [70,70,-63];

loc_2 = [750,1750,500,1500;...
    750,1750,500,1500;...
    550,1550,700,1700];

sl_2 = [400,500,350,450;...
    440,540,540,640;...
    500,600,515,615];

th_3 = [22,-50];

loc_3 = [750,1750,750,1750;...
    750,1750,750,1750];
```

```
sl_3 = [580,680,450,550;...
    500,600,275,375];

th_4 = [10,30,40,-30,-30];

loc_4 = [500,1500,650,1650;...
    750,1750,750,1750;...
    750,1750,750,1750;...
    750,1750,750,1750;...
    750,1750,750,1750];

sl_4 = [290,390,465,490;...
    280,380,570,620;...
    800,900,575,645;...
    600,700,400,500;...
    600,700,560,620];

th_5 = [-30,-65];

loc_5 = [500,1500,750,1750;...
    800,1800,550,1550];

sl_5 = [750,850,450,500;...
    375,475,480,520];

th_6 = [-13,42,-75];

loc_6 = [550,1550,300,1300;...
    1050,2050,650,1650;...
    350,1350,200,1200];

sl_6 = [610,710,430,480;...
    480,580,440,490;...
    475,575,480,550];
%%

th = {th_1 th_2 th_3 th_4 th_5 th_6};
loc = {loc_1 loc_2 loc_3 loc_4 loc_5 loc_6};
sl = {sl_1 sl_2 sl_3 sl_4 sl_5 sl_6};


for j = 1:length(th)
figure()
Mo_pk = [];
Mo_pk_avg = [];
Mo_pk_SEM = [];
Mo_ctr = [];
Mo_ctr_avg = [];
Mo_ctr_SEM = [];
Mo_bg_all = {};
Mo_pk_all = {};
Mo_ctr_all = {};
for i = 1:length(th{j})
    % Rotate image
```

```
    temp = imrotate(MoSe{j},th{j}(i));
    MoSe_th(:,:,i) = temp(loc{j}(i,1):loc{j}(i,2),loc{j}(i,3):loc{j}(i,4));

    % Plot rotated image
    subplot(2,length(th{j}),i)
    imagesc(MoSe_th(:,:,i))
    line([sl{j}(i,3) , sl{j}(i,3)],[sl{j}(i,1),sl{j}(i,2)],'Color','red');
    line([sl{j}(i,4) , sl{j}(i,4)],[sl{j}(i,1),sl{j}(i,2)],'Color','red');

    % Calculate background
    Mo_bg_all{i} =
mean([mean(MoSe_th(sl{j}(i,1):sl{j}(i,1)+10,sl{j}(i,3):sl{j}(i,4),i)) ;
mean(MoSe_th(sl{j}(i,2)-10:sl{j}(i,2),sl{j}(i,3):sl{j}(i,4),i))]);

    % Plot slice
    subplot(2,length(th{j}),i+length(th{j}))
    plot(MoSe_th(sl{j}(i,1):sl{j}(i,2),sl{j}(i,3):sl{j}(i,4),i)-
Mo_bg_all{i})


    % Caclulate peak, contrast, and add to plot
    Mo_pk_all{i} =
double(max(MoSe_th(sl{j}(i,1):sl{j}(i,2),sl{j}(i,3):sl{j}(i,4),i)-
Mo_bg_all{i}));
    Mo_pk_avg(i) = mean(Mo_pk_all{i});
    Mo_pk_SEM(i) = std(Mo_pk_all{i})/sqrt(length(Mo_pk_all{i}));

    Mo_ctr_all{i} = (Mo_pk_all{i}+Mo_bg_all{i})./Mo_bg_all{i};
    Mo_ctr_avg(i) = mean(Mo_ctr_all{i});
    Mo_ctr_SEM(i) = std(Mo_ctr_all{i})/sqrt(length(Mo_ctr_all{i}));

    ylim([-5 Mo_pk_avg(i)*1.25])
    text(5,(Mo_pk_avg(i)*1.25)-
(Mo_pk_avg(i)*.125),['Contrast',newline,sprintf('%.3f %c %.3f',Mo_ctr_avg(i
),177,Mo_ctr_SEM(i))] );
    text(45,(Mo_pk_avg(i)*1.25)-
(Mo_pk_avg(i)*.125),['Peak',newline,sprintf('%.3f %c %.3f',Mo_pk_avg(i),177
,Mo_pk_SEM(i))]);
end
Mo_DF_Intensity = [Mo_DF_Intensity Mo_pk_avg];
Mo_Intensity_err = [Mo_Intensity_err Mo_pk_SEM];

Mo_DF_Contrast = [Mo_DF_Contrast Mo_ctr_avg];
Mo_Contrast_err = [Mo_Contrast_err Mo_ctr_SEM];
end

%% Functions
function [SEM] = StErMean(data)
    SEM = mean(data)./sqrt(length(data));
end
```

Appendix 2: MATLAB Script for Spectra Processing

```
% Taken from upper and lower bounds when files opened in WinSpec
lambda_list = [720 702.18 737.77;...
    750 732.41 767.53;...
    790 772.73 807.19;...
    820 802.98 836.93;...
    850 835 865;...
    880 863 896;...
    910 893.81 926.06;...
    940 924.1 955.76;...
    970 954.41 985.43;...
    1000 985 1015];

% Spectral y integration values (width of emission spot)
spec_yint = 240:300;

% Pixel values of slit open to 7mm (June 2021) THIS VALUE CHANGES
slit = 915:1094;

burnin = {};

filenames={'HeNe_1.6K_3000uW_Spot1_720nm_300s_650LP.SPE' ...
    'HeNe_1.6K_3000uW_Spot1_750nm_300s_650LP_2.SPE' ...
    'HeNe_1.6K_3000uW_Spot1_790nm_300s_650LP_6_24.SPE' ...
    'HeNe_1.6K_3000uW_Spot1_820nm_300s_650LP_6_24.SPE' ...
    'HeNe_1.6K_3000uW_Spot1_850nm_300s_650LP_6_24.SPE' ...
    'HeNe_1.6K_3000uW_Spot1_880nm_300s_650LP_6_24.SPE' ...
    'HeNe_1.6K_3000uW_Spot1_910nm_300s_650LP_6_24_2.SPE'};

    lambdas = [720 750 790 820 850 880 910];
    exp_lambda = zeros(length(lambdas),2);
    for i = 1:length(lambdas)
        loc = find(lambda_list == lambdas(i));
        exp_lambda(i,1:2) = lambda_list(loc,2:3);
    end
    %exp_lambda_range = [];
    %exp_lambda_range(1:length(exp_lambda)) = diff(exp_lambda,1,2);
    exp_ev = 1239.84193./exp_lambda;

    Spot1_int = {[],[],[]};
    Spot1_xvals = {[],[],[]};

%Read all images
raw_images_d = zeros(512,2048,'int16');

for i = 1:length(filenames)
    [image_i,info_i] = readSPE(filenames{i});
    %raw_images(:,:,i) = image_i;
    raw_images_d(:,:,i) = double(image_i);
    bgs(i) = mean(mean(raw_images_d(1:50,1:50,i)));
    burnin{i} = ((mean(raw_images_d(1:50,slit,i))) - bgs(i));
end
```

```
% Rotate Images and background subtraction
    % th was found using the full image, need a better way of doing this
    th = atand((373-323)/(9009-5553));

        flat_images = [];
        raw_gradients = [];

    for i = 1:length(filenames)
        flat_images(:,:,i) = imrotate(raw_images_d(:,:,i),th) - bgs(i);
        flat_images(:,slit,i) = flat_images(:,slit,i) - burnin{i};
        temp = flat_images(:,:,i);
        temp(temp<0) = 0;
        flat_images(:,:,i) = temp;
        raw_gradients(:,:,i) = imgradient(flat_images(:,:,i));
    end

% Remove Cosmic Rays

    for i = 1:length(filenames)
        temp = flat_images(:,:,i);
        temp_grad = raw_gradients(:,:,i);
        %temp(temp_grad(240:290,:) > 50.*mean(mean(temp_grad(240:290,:))))
= mean(mean(temp_grad(240:290,:)));
        temp(temp_grad(:,:) > 15.*mean(mean(temp_grad(spec_yint,:)))) =
mean(mean(temp(spec_yint,:)));
        flat_images(:,:,i) = temp;
    end

% Integrate and Plot
    chop = 20;
    overlap = ones(1,length(filenames)).*250;

figure()
    title('Spot 1 Emission','FontSize',24)
    xlabel('Energy (eV)','FontSize',24)
    ylabel('Counts')
    for j = 1:ceil(length(filenames)/length(lambdas))
    for i = 1:length(lambdas)
        if i == 1
        integrated(i,:) = sum(flat_images(spec_yint,:,i+((j-
1)*length(lambdas))));
        else
        %overlap_interp = linspace(1,0,overlap(i-1)+1);
        integrated(i,:) = sum(flat_images(spec_yint,:,i+((j-
1)*length(lambdas))));
        %integrated(i,chop:chop+overlap(i-1)) = ((1-
overlap_interp).*integrated(i-1,end-chop-overlap(i-1):end-chop) +
(overlap_interp).*integrated(i,chop:chop+overlap(i-1))).*1.05;
        end
    %end-chop-overlap(i-1):end-chop
        hold on
        lambda_temp =
linspace(exp_lambda(i,1),exp_lambda(i,2),length(integrated(i,:)));
```

```
        ev_temp =
linspace(exp_ev(i,1),exp_ev(i,2),length(integrated(i,:)));

        plot(ev_temp(chop:end-chop),integrated(i,chop:end-
chop),'Color',colors(j,1:3))
        if i < 5
        Spot1_int{j} = [Spot1_int{j} integrated(i,chop:end-chop)];
        Spot1_xvals{j} = [Spot1_xvals{j} ev_temp(chop:end-chop)];
        else
            Spot1_int{j} = [Spot1_int{j} integrated(i,chop:end-chop)-50];
            Spot1_xvals{j} = [Spot1_xvals{j} ev_temp(chop:end-chop)];
        end
    end %Integrating and Plotting
    end
    %xline(1.68686);
    %xline(1.50284);
    hold off
```